Computers and Mathematics with Applications 64 (2012) 2520–2543

Contents lists available at SciVerse ScienceDirect

Computers and Mathematics with Applications

journal homepage: www.elsevier.com/locate/camwa

Solution of the 3D-Helmholtz equation in exterior domains using spherical harmonic decomposition

G. Garate [a,*], E.G. Vadillo [b], J. Santamaria [b], D. Pardo [c,d]

[a] Department of Applied Mathematics, University of the Basque Country (University of the Basque Country UPV/EHU), Donostia, Spain
[b] Department of Mechanical Engineering, University of the Basque Country UPV/EHU, Bilbao, Spain
[c] Department of Applied Mathematics, Statistics and Operational Research, University of the Basque Country UPV/EHU, Leioa, Spain
[d] Ikerbasque, Bilbao, Spain

ARTICLE INFO

Article history:
Received 10 January 2012
Received in revised form 26 April 2012
Accepted 13 June 2012

Keywords:
Helmholtz equation
Radiation
Scattering
Infinite domains

ABSTRACT

This work is devoted to a finite element formulation for the Helmholtz equation in exterior domains. The proposed formulation uses a separation of variables, combining a 2D FE discretization on an intermediate spherical boundary and an 'a priori' analytical pattern for the radial direction. Using the analytical radial pattern and the series expansion of trial and test functions in terms of spherical harmonics, an efficient semi-analytical technique is obtained for the direct calculation of the global FE matrices. The accuracy and reliability of the formulation are illustrated through numerical examples of radiation and scattering in the exterior domain.

1. Introduction

The aim of this work is to obtain a simple finite element formulation capable to approximate radiation and scattering acoustic problems that extend to an infinite domain. Several strategies have been developed in the past to properly solve wave propagation problems in unbounded domains, which include Boundary Elements (BEs), Infinite Elements (IEs), Absorbing Boundary Conditions (ABCs), non-reflecting boundary conditions (NRBCs) and Perfect Matched Layer (PML) techniques.

The BE method [1,2] has been the classical way of solving the scattering problem. The main advantages of the BE method arise from the fact that only the boundary (or boundaries) of the domain of the PDE requires sub-division. Thus, the dimension of the problem is effectively reduced by one: for example, an equation governing a three-dimensional region is transformed into a surface integral. BE techniques have also been successfully coupled to FE methods [3]. The main shortcomings of the BE methods are their high computational cost at high frequencies and the non-uniqueness of the solution at certain characteristic frequencies [4].

The IE approach intends to solve the problem from inside the theoretical corpus of the FE method. After the introduction of the original formulation by Bettess [5], other IE techniques have been developed. Some of them use mapped infinite elements, such as those by Astley et al. [6]; others use a FE/IE methodology and a *hp* adaptivity (adding degrees of freedom for the interpolation in the radial direction) and have achieved good results, such as those by Gerdes et al. [7,8].

Other mesh truncation methods include ABC [9–12], NRBC [13,14] and PML methods [15–18]. In these, the analysis is made by enclosing the scatterer within a boundary or a layer of a given thickness at a prescribed distance from the scatterer, enclosing the domain of interest. The geometry is typically spherical or rectangular. The drawback of truncation methods is

* Corresponding author. Tel.: +34 943 017223.
E-mail address: gorka.garate@ehu.es (G. Garate).

0898-1221/$ – see front matter © 2012 Elsevier Ltd. All rights reserved.
doi:10.1016/j.camwa.2012.06.010

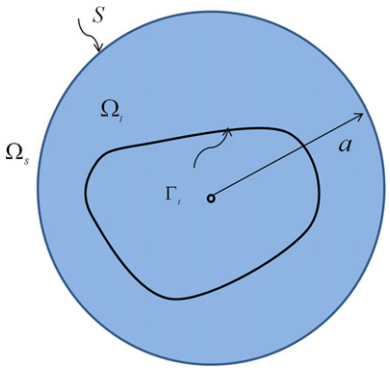

Fig. 1. Subdomains Ω_i and Ω_s and dividing surface S.

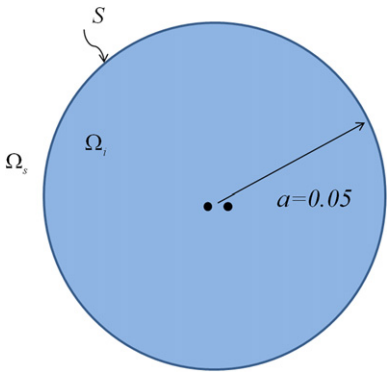

Fig. 2. The geometrical model used.

the high number of extra degrees of freedom that have to be used within the domain of interest or inside the PML; besides, special post-processing techniques are needed for the calculus of the solution outside the boundary or the layer. For ABC, accuracy is an added problem.

Other techniques combine the advantages of FE and BE methods; one of these is the scaled boundary finite element method [19–21], usually employed in elastodynamics, and others [22,23]. In this method, the boundary is discretized with surface finite elements, yielding a reduction of the spatial dimension by one, while the radiation condition at infinity is satisfied exactly; in addition, the method combines the advantages of both FE and BE methods: in the directions parallel to the boundary, the weighted-residual approximation of finite elements applies, leading to convergence in the ordinary FE sense; in the third (radial) direction, however, the procedure is analytical. A comparison among the different methods can be found in [24].

In this paper, an approximation of the FE/BE combination type is presented. The inspiration of the method comes from classical theoretical acoustics [25,26]. In the area concerning radiation of sound, theoretical physics usually analyzes the case of radiation from spheres, studying the sound waves caused by the known vibration pattern of a sphere (not necessarily small). The radiated pressure is expressed as a series of Hankel and Legendre functions and coefficients that can be determined using the radiation pattern on the sphere.

The idea of the method presented here is to split into two the entire infinite domain using a spherical surface, and calculate the pressure in the outer domain as a radiation from *that* dividing sphere. The outside pressure pattern will only depend on the nodal values of the pressure *on* the sphere (which are unknowns) and the 2D linear FEM functions (which we know). In order to minimize the number of degrees of freedom, we will place the dividing surface as close as possible to the radiator/scatterer; that is, in the near field. In the results presented the dividing sphere will always be located closer than a sixth of a wavelength from the scatterer.

Once the division is performed, two coupled FE formulations arise.

- In the inner subdomain, an ordinary 3D finite mesh is generated; there, any radiating/scattering surface, acoustic source or coupling with other media can be introduced.
- In the outer subdomain, the faces of the elements of the inner mesh lying on the dividing sphere are used as a 2D discretization to make two different interpolations. On the radial direction, an analytical pattern – based on the known analytical solution for the Helmholtz equation – is used, which allows for the radiation boundary condition at infinity to be satisfied exactly; on the zenithal and azimuthal directions a series expansion (of infinite number of terms) of the customary FE basis functions is used.

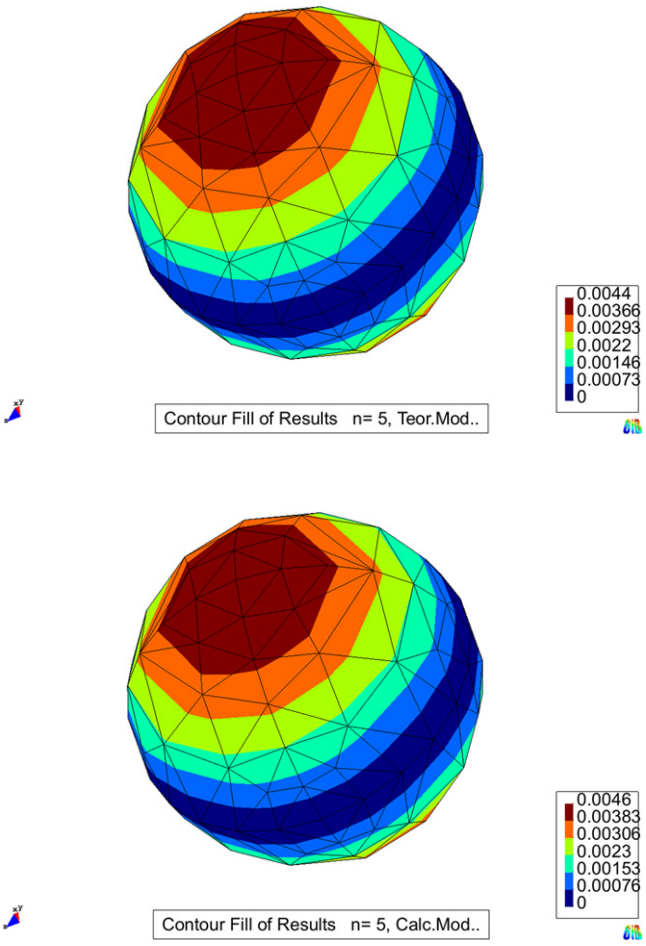

Fig. 3. Analytical and calculated pressure moduli. Coarse mesh.

The main advantage of the proposed method over BEM is that our method does not perform any integration during the calculation, because the matrices are calculated analytically based on previously calculated integrals of Hankel functions and spherical harmonics. Besides that advantage, it allows for a faster post-processing by simplifying the calculus (all post-process calculations are reduced to simple matrix products).

Comparing it to IE, the infinite element theory does indeed allow for spheroidal truncation; but the truncation must be made in the far field; or, if done in the near field, additional d.o.f. must be added in the radial direction. The formulation presented is able to truncate the domain in the near field (in the examples presented the largest distance from the source has been a sixth of the wavelength) without adding any d.o.f. to the FEM model.

The indisputable advantage of PML over the presented method is the ability of dealing with non-homogeneous media; its main drawbacks are: (a) A PML does not provide results outside the truncation surface (outer-domain); and (b), additional d.o.f. are necessarily added within the PML, whereas the presented method adds zero d.o.f. In summary: the main advantage of the proposed method is that the dividing surface can be located as close as possible to the radiator/scatterer without adding any d.o.f. to the model, and at the same time, it provides an efficient way to compute the solution in the outer-domain.

The summation over the infinite series is obviously truncated by necessity; the crucial issue is to decide how many terms must be taken to ensure a prescribed accuracy. In the examples presented in this paper, the largest number of terms reached is 40, and that happens for the highest frequency used, namely, $k = 10$. Furthermore, the presented examples suggest that just 20 terms in the series are enough, since the accuracy is not significantly improved by adding more terms. Thus, the number of significant terms in practice seems to be quite small.

The proposed truncation method does not add unknowns to the system, which is a desirable property that is not satisfied by PMLs neither by IE. However, our truncation method increases the connectivity of those unknowns sitting at the boundary, generating a dense submatrix. While the cost associated to solve that dense submatrix may seem outrageously expensive, this is not always the case, and the proposed method becomes useful in a number of applications. For example, when using a direct solver, the final LU factorization step typically requires a solution of a dense system whose size is that of

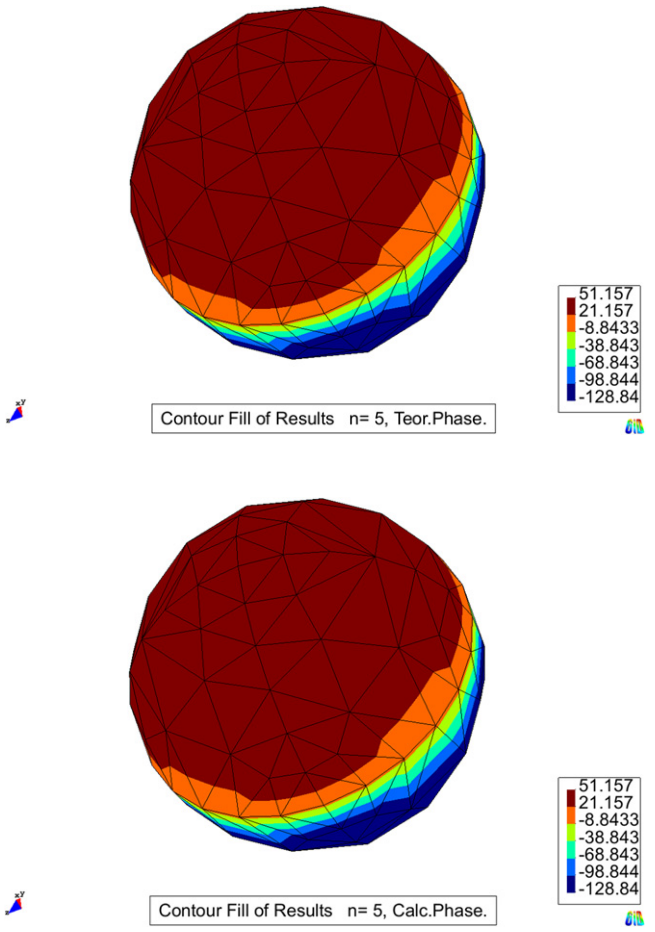

Fig. 4. Analytical and calculated pressure phases. Coarse mesh.

a 2D cross-section of the original domain. If this cross-section contains more unknowns than those sitting at the boundary, then the cost of adding the truncation method will be significantly lower than that of solving the original system without the truncation method. Notice that this situation often occurs when we consider geometrically complex scatterers inside the domain of interest. Moreover, this observation suggests the use of rather coarse grids on the boundary of the domain of interest.

Alternatively, in those applications where the discretization requires a heavily populated boundary, the matrix resulting from the proposed truncation method can be efficiently solved by using ideas of H-matrices [27], such as those recently developed by Schmitz and Ying [28].

In this paper only the formulation for the outer subdomain Ω_s will be detailed; for the ordinary 3D FE formulation in the inner subdomain Ω_i the reader is referred to the large existing bibliography [29–31].

Section 2 shows the resolution of the Helmholtz equation in spherical coordinates. That is the pattern of the solution obtained which will be used for the trial functions. Section 3 expounds the formulation of the method: in Section 3.1 the weak formulation and the sets of trial and test functions are defined; Section 3.2 shows the series decomposition of the basis functions in terms of spherical harmonics; finally, Section 3.3 details the final formulas for the direct calculation of the global stiffness and mass matrices. The applied approximation leads to analytically compute integrals, and the *global* matrices of the outer subdomain are directly calculated and assembled to the matrices obtained for the inner subdomain. The fact that only the evaluations of analytical functions and single matrix products must be performed – together with the minimization of the number of d.o.f. achieved in the inner domain – accounts for the efficiency of the method. Another advantageous feature is that the use of trial functions with continuous derivatives avoids the need of smoothing in the calculations of the values of the derivatives at the nodes and any post-process magnitude related to them, which are calculated very quickly, by simple matrix products. Section 4 contrasts the numerical results obtained with two analytical results: one of radiation (dipole) and one of scattering (plane wave striking a rigid sphere). Contour plots of modulus, phase and local relative error are shown, together with the H^1 relative norms obtained varying the order of the approximation. The results demonstrate the accuracy and reliability of the method. Finally, Section 5 enumerates the main conclusions and future lines of work of the authors.

2. The Helmholtz equation

2.1. The analytical solution in spherical coordinates

The second order wave equation in spherical coordinates is

$$\frac{1}{r^2}\frac{\partial}{\partial r}\left(r^2\frac{\partial u}{\partial r}\right)+\frac{1}{r^2\sin\theta}\frac{\partial}{\partial\theta}\left(\sin\theta\frac{\partial u}{\partial\theta}\right)+\frac{1}{r^2\sin^2\theta}\frac{\partial^2 u}{\partial\varphi^2}-\frac{1}{c^2}\frac{\partial^2 u}{\partial t^2}=S, \tag{1}$$

where S is the source function.

The Helmholtz equation is obtained by setting the functions as periodical, of the form $u(r,\theta,\varphi,t)=p(r,\theta,\varphi)\,e^{i\omega t}$:

$$\frac{1}{r^2}\frac{\partial}{\partial r}\left(r^2\frac{\partial p}{\partial r}\right)+\frac{1}{r^2\sin\theta}\frac{\partial}{\partial\theta}\left(\sin\theta\frac{\partial p}{\partial\theta}\right)+\frac{1}{r^2\sin^2\theta}\frac{\partial^2 p}{\partial\varphi^2}+k^2p=s, \tag{2}$$

where $k=\omega/c$ is the wave number. We will summarize this equation as

$$\Delta p+k^2p=s. \tag{3}$$

The classical analytical solution of the Helmholtz equation in spherical coordinates [26] is based on a separation of variables r, θ and φ. The solution obtained can be expressed as a combination of Legendre polynomials and spherical Hankel functions. The Sommerfeld radiation condition

$$\left|\frac{\partial p}{\partial\vec{n}}-ikp\right|=\mathrm{O}\left(\frac{1}{r^2}\right) \tag{4}$$

eliminates the Hankel functions of the second kind, and therefore the solution can be written as follows:

$$p(r,\theta,\varphi)=\sum_{m=0}^{\infty}h_m(k,r)\sum_{n=0}^{m}P_m^n(\cos\theta)\left(A_{mn}\cos(n\varphi)+B_{mn}\sin(n\varphi)\right), \tag{5}$$

where the radial part of the solution is given by the spherical Hankel functions of the first kind

$$h_m(k,r)=e^{ikr}\frac{i^{-(m+1)}}{kr}\sum_{s=0}^{m}\frac{(m+s)!}{(m-s)!s!}\left(\frac{i}{2k}\right)^s r^{-s}, \tag{6}$$

and the azimuthal and zenithal parts are defined by the functions cos and sin and the functions

$$P_m^n(x)=(-1)^n\left(1-x^2\right)^{\frac{n}{2}}\frac{d}{dx^n}P_m(x), \tag{7}$$

which are the derivatives of the Legendre polynomials of degree m

$$P_m(x)=\frac{1}{2^m m!}\left[\frac{d}{dx^m}\left(x^2-1\right)^m\right]. \tag{8}$$

Coefficients A_{mn} and B_{mn} of solution (5) are to be determined applying the boundary conditions.

3. FE formulation

The entire space R^3 is split into two subdomains Ω_i and Ω_s by a dividing sphere S of radius a, as illustrated in Fig. 1. The radiator/scatterer can be located in the inner subdomain; in the figure, it is designated as Γ_i.

In the inner subdomain Ω_i an ordinary 3D FE formulation is used; in the outer subdomain Ω_s, we will employ the pattern of the analytical solution (5), by using a 2D interpolation in the azimuthal and zenithal directions and the radial solution expressed in terms of Hankel functions (6). This allows the integrals of the weak formulation to be calculated analytically.

3.1. Weak formulation

The strong form of the Boundary Value Problem comprises the Helmholtz equation (3) and the Sommerfeld radiation condition (4) at infinity. The first version of the weak form is obtained by multiplying the Helmholtz equation by a test

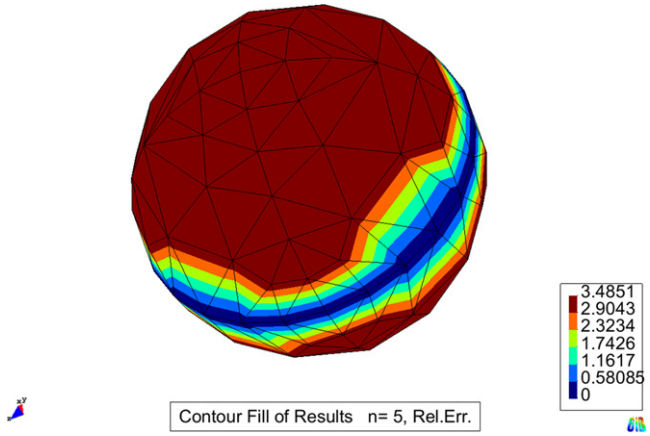

Fig. 5. The relative error in %. Coarse mesh.

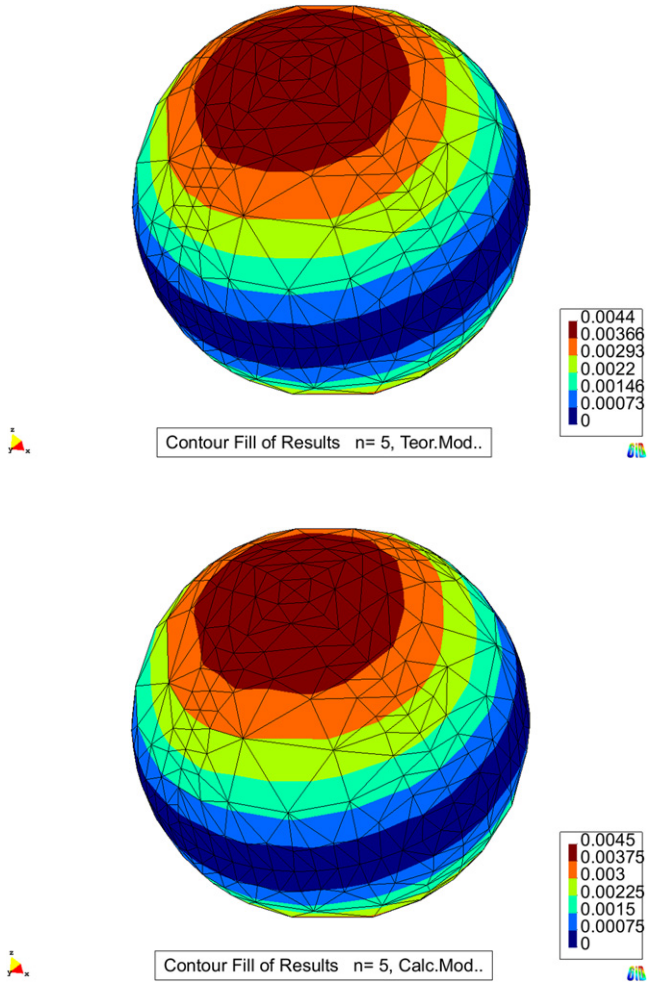

Fig. 6. Analytical and calculated pressure moduli. Fine mesh.

function $w(\vec{x})$, integrating over the domain outside the dividing surface and integrating by parts. We arrive at the formulation

$$\iiint_{\Omega_s} \vec{\nabla} w \vec{\nabla} p d\Omega - k^2 \iiint_{\Omega_s} w p d\Omega - \iint_{S_\gamma} w \frac{\partial p}{\partial \vec{n}} ds = \iiint_{\Omega_s} w s d\Omega \quad \forall w\left(\vec{x}\right) \in V, \tag{9}$$

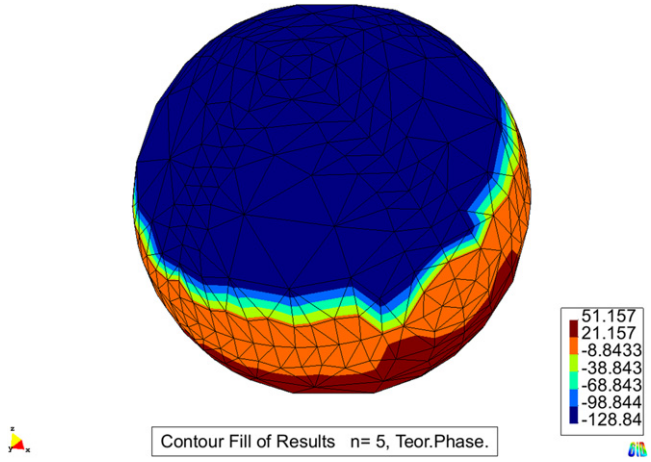

Fig. 7. Analytical and calculated pressure phases. Fine mesh.

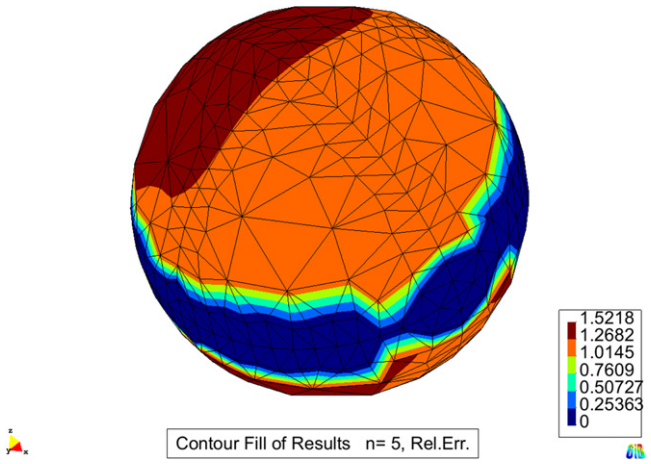

Fig. 8. The relative error in %. Fine mesh.

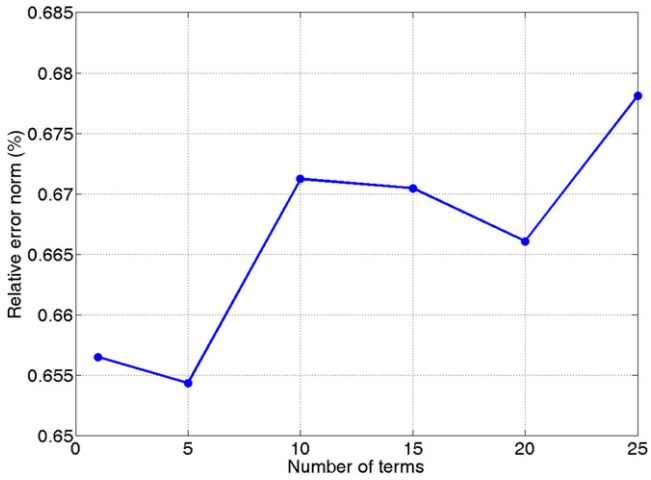

Fig. 9. The relative error (%) in the H^1 norm. Coarse mesh.

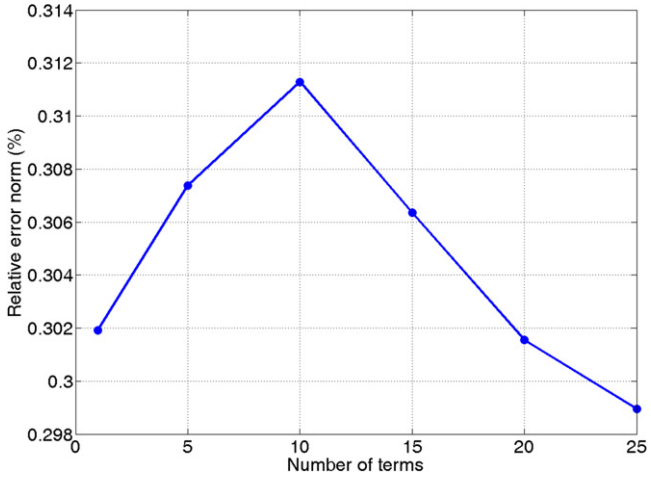

Fig. 10. The relative error (%) in the H^1 norm. Fine mesh.

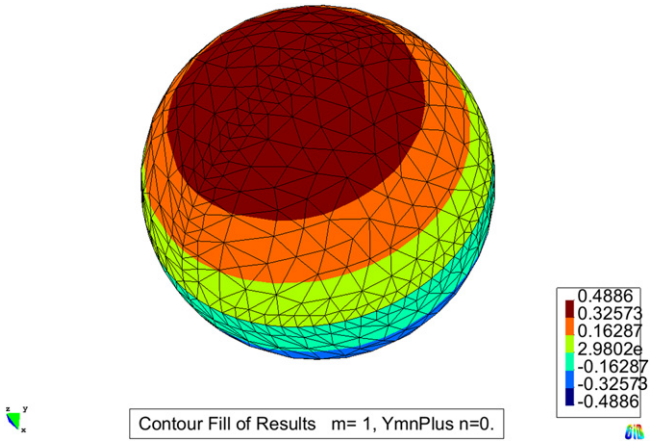

Fig. 11. Spherical harmonic Y_{10}^1.

where S_γ is the truncating sphere with radius $r = \gamma$, and the set $V = \left\{w \in H^1 \mid w = 0 \text{ on } S_\gamma\right\}$. Rewriting the Sommerfeld radiation condition (4) we obtain the expression

$$\frac{\partial p}{\partial r} = ikp + \phi\left(\vec{x}\right), \tag{10}$$

where $\phi\left(\vec{x}\right) = \mathrm{O}\left(r^{-2}\right)$ is an unknown function. Substituting for $\partial p/\partial \vec{n} = \partial p/\partial r$ in Eq. (9) we obtain

$$\iiint_{\Omega_s} \vec{\nabla} w \vec{\nabla} p d\Omega - k^2 \iiint_{\Omega_s} w p d\Omega - ik \iint_{S_\gamma} w p ds = \iint_{S_\gamma} w \phi ds + \iiint_{\Omega_s} w s d\Omega \quad \forall w\left(\vec{x}\right) \in V. \tag{11}$$

In order to pass with γ to ∞, several strategies have been used in the past. The first is to include the Sommerfeld condition into the definition of the spaces. This is the line followed by Leis [32]. The idea is to restrict the space of the solution functions to a weighted subspace in which the value after applying the operator is in a $L^2\left(\Omega_s\right)$ space. The conclusion is that the integrals over S_γ vanish in the limit $r \to \infty$.

The second strategy follows [33]. There, both solution and test functions are selected from $H^1\left(\Omega_s\right)$, so that the former satisfies the Sommerfeld condition and the gradients of both functions are square-integrable; but the difference in this case is that the integral over S_γ involving the radiation pattern does *not* vanish in the limit.

In the formulation presented in this paper trial functions p have the form of Eq. (5) and constitute a subspace of space $C^\infty\left(\Omega_s\right)$ which will be denoted by $C_p^\infty\left(\Omega_s\right)$. Since Hankel spherical functions of the first kind directly satisfy the Sommerfeld condition, we only need to select test functions $w\left(r, \theta, \varphi\right)$ to ensure the square-integrability of the integrands of the weak form.

At this stage, the final variational formulation reads as follows:

$$\left\{\begin{array}{l}\text{Find } p \in C_p^\infty\left(\Omega_s\right) \text{ such that} \\ \iiint_{\Omega_s} \vec{\nabla} w \vec{\nabla} p ds - k^2 \iiint_{\Omega_s} w p ds = \iiint_{\Omega_s} w s d\Omega \quad \forall w \in C_w^\infty\left(\Omega_s\right)\end{array}\right\}, \tag{12}$$

where $C_w^\infty\left(\Omega_s\right)$ is the space of functions with finite inner product

$$b\left(p, w\right)^1 = \iiint_{\Omega_s} \vec{\nabla} w \vec{\nabla} p ds - k^2 \iiint_{\Omega_s} w p ds \quad \forall p \in C_p^\infty\left(\Omega_s\right). \tag{13}$$

The set of selected test functions $w\left(r, \theta, \varphi\right) \in C_w^\infty\left(\Omega_s\right)$ selected will be detailed in Section 3.3.

3.2. Spherical harmonic decomposition of the basis functions

The spherical harmonics are defined as follows [25,26]:

$$Y_m\left(\theta\right) = Y_{m0}^1\left(\theta, \varphi\right) = k_{m0} P_m\left(\cos\theta\right) \tag{14a}$$

$$Y_{mn}^1\left(\theta, \varphi\right) = k_{mn} \cos\left(n\varphi\right) P_m^n\left(\cos\theta\right) \tag{14b}$$

$$Y_{mn}^{-1}\left(\theta, \varphi\right) = k_{mn} \sin\left(n\varphi\right) P_m^n\left(\cos\theta\right) \tag{14c}$$

where $P_m^n\left(\cos\theta\right)$ are the Legendre functions and the coefficient k_{mn} is

$$k_{mn} = \sqrt{\frac{\left(2m+1\right)\left(m-n\right)!}{2^{(2-\mathrm{sign}(n))}\pi\ \left(m+n\right)!}}. \tag{15}$$

The set of spherical harmonics (14) is a complete mutually orthonormal set of functions in terms of coordinates θ, φ, with the scalar product

$$\left(Y_{mn}^\sigma\left(\theta, \varphi\right), Y_{lk}^\tau\left(\theta, \varphi\right)\right)_{\Gamma_s} = \int_0^{2\pi} d\varphi \int_0^\pi Y_{mn}^\sigma\left(\theta, \varphi\right) Y_{lk}^\tau\left(\theta, \varphi\right) \sin\theta d\theta. \tag{16}$$

Now let us see how the spherical harmonics are used for the interpolation. A classical 3D FE interpolation would read as follows:

$$p^h\left(r, \theta, \varphi\right) = \sum_{j=0}^{n_s} M_j\left(r, \theta, \varphi\right) p_j \tag{17a}$$

$$w^h \in V^h = \mathrm{span}\left\{M_j^*\left(r, \theta, \varphi\right)\ \forall j \in \eta_s\right\} \tag{17b}$$

for the solution and test functions respectively. In (17) n_s is the total number of nodes, and η_s is the number of nodes at which no Dirichlet condition is imposed. The basic idea of the present work is to separate the variables of functions $M_j\left(r, \theta, \varphi\right)$

and $M_j^*(r,\theta,\varphi)$ using the radiation pattern on the dividing sphere given by the 2D FE interpolation functions and the nodal values:

$$p^h(a,\theta,\varphi) = \sum_{j=0}^{n_s} N_j(\theta,\varphi)\, p_j. \tag{18}$$

Substituting the 2D interpolation functions $N_j(\theta,\varphi)$ for a series of the aforementioned spherical harmonics $Y_{mn}^{\sigma}(\theta,\varphi)$ in the form

$$N_j(\theta,\varphi) = \sum_{m=0}^{\infty}\sum_{n=0}^{m}\left(A_{mn}^j Y_{mn}^1 + B_{mn}^j Y_{mn}^{-1}\right), \tag{19}$$

where coefficients A_{mn}^j and B_{mn}^j can be computed using the orthogonality of the spherical harmonics:

$$A_{mn}^j = \int_0^{2\pi} d\varphi \int_0^{\pi} N_j(\theta,\varphi)\, Y_{mn}^1(\theta,\varphi)\sin\theta d\theta \tag{20a}$$

$$B_{mn}^j = \int_0^{2\pi} d\varphi \int_0^{\pi} N_j(\theta,\varphi)\, Y_{mn}^{-1}(\theta,\varphi)\sin\theta d\theta. \tag{20b}$$

Extending the radius from a to infinity in (18), the interpolation in the outer infinite domain is given by

$$p^h(r,\theta,\varphi) = \sum_{j=1}^{n_s} M_j(r,\theta,\varphi)\, p_j, \tag{21}$$

where the summation over j is performed over the nodes, and FE interpolation functions are given by

$$M_j(r,\theta,\varphi) = \sum_{m=0}^{\infty} h_m(k,r)\sum_{n=0}^{m}\left(A_{mn}^j Y_{mn}^1(\theta,\varphi) + B_{mn}^j Y_{mn}^{-1}(\theta,\varphi)\right), \tag{22}$$

where the summations over m and n are performed over the spherical harmonics, and the functions $h_m(k,r)$ are the Hankel functions of (6). In a similar way, functions $M_j^*(r,\theta,\varphi)$ are given by

$$M_j^*(r,\theta,\varphi) = \sum_{m=0}^{\infty} w_m(k,r)\sum_{n=0}^{m}\left(A_{mn}^j Y_{mn}^1(\theta,\varphi) + B_{mn}^j Y_{mn}^{-1}(\theta,\varphi)\right), \tag{23}$$

where functions $w_m(k,r)$ are weight functions that will be detailed in Section 3.3.1.

Coefficients of the integrals in (20) are in fact numerically approximated by means of numerical surface integrals over S:

$$A_{mn}^i = \frac{1}{a^2}\iint_S N_i(\theta,\varphi)\, Y_{mn}^1(\theta,\varphi)\, ds \tag{24a}$$

$$B_{mn}^i = \frac{1}{a^2}\iint_S N_i(\theta,\varphi)\, Y_{mn}^{-1}(\theta,\varphi)\, ds. \tag{24b}$$

3.3. FE formulation

3.3.1. Definition of trial and test functions

Substituting the interpolation and test functions given in (22) and (23) in the series expansion (21), the solution function p^h and its derivatives outside the dividing surface can be written as

$$\begin{aligned}
p^h(r,\theta,\varphi) &= \sum_{j=1}^{n_s}\left(\sum_{d=0}^{\infty} h_d(k,r)\sum_{l=0}^{d}\left(A_{dl}^j Y_{dl}^1(\theta,\varphi) + B_{dl}^j Y_{dl}^{-1}(\theta,\varphi)\right)\right) p_j \\
\frac{\partial p^h}{\partial r} &= \sum_{j=1}^{n_e}\left(\sum_{d=0}^{\infty}\frac{\partial h_d}{\partial r}\sum_{l=0}^{d}\left(A_{dl}^j Y_{dl}^1 + B_{dl}^j Y_{dl}^{-1}\right)\right) p_j \\
\frac{\partial p^h}{\partial \theta} &= \sum_{j=1}^{n_s}\left(\sum_{d=0}^{\infty} h_d(k,r)\sum_{l=0}^{d}\left(A_{dl}^j \frac{\partial Y_{dl}^1}{\partial\theta} + B_{dl}^j \frac{\partial Y_{dl}^{-1}}{\partial\theta}\right)\right) p_j \\
\frac{\partial p^h}{\partial \varphi} &= \sum_{j=1}^{n_s}\left(\sum_{d=0}^{\infty} h_d(k,r)\sum_{l=0}^{d}\left(A_{dl}^j \frac{\partial Y_{dl}^1}{\partial\varphi} + B_{dl}^j \frac{\partial Y_{dl}^{-1}}{\partial\varphi}\right)\right) p_j.
\end{aligned} \tag{25}$$

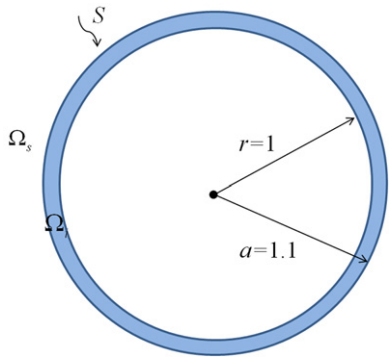

Fig. 12. The geometrical model used.

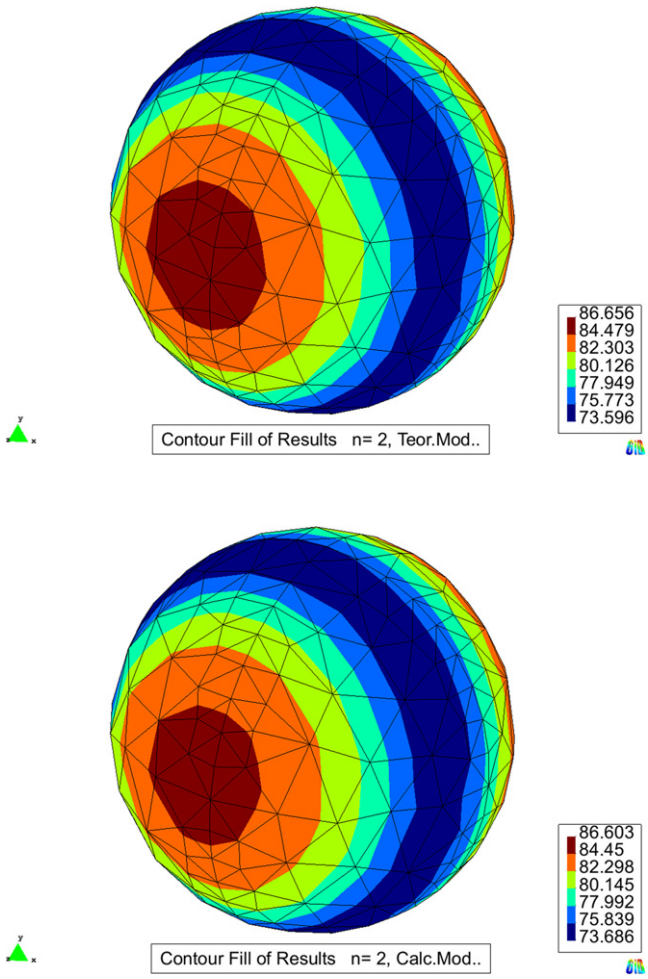

Fig. 13. Analytical and calculated pressure moduli ($k = 1$). Coarse mesh.

Now using series expansion (23), for the space of test functions of (13) outside the dividing surface we have the expression:

$$C_w^{\infty}(\Omega_s)^h = \text{span}\left\{M_i^*(r,\theta,\varphi)\right\} \quad \forall i \in \eta_s$$

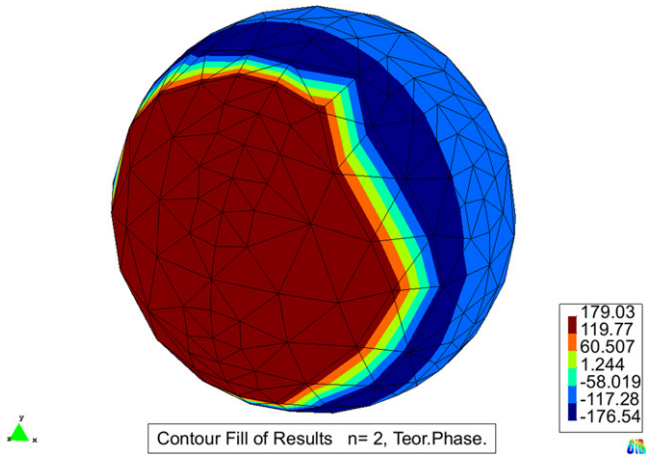

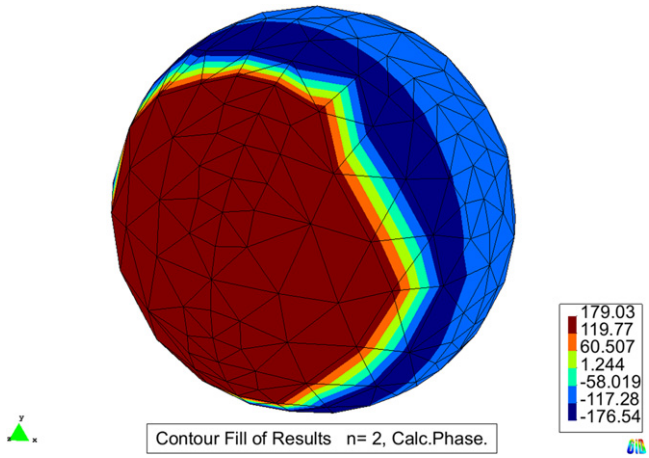

Fig. 14. Analytical and calculated pressure phases ($k = 1$). Coarse mesh.

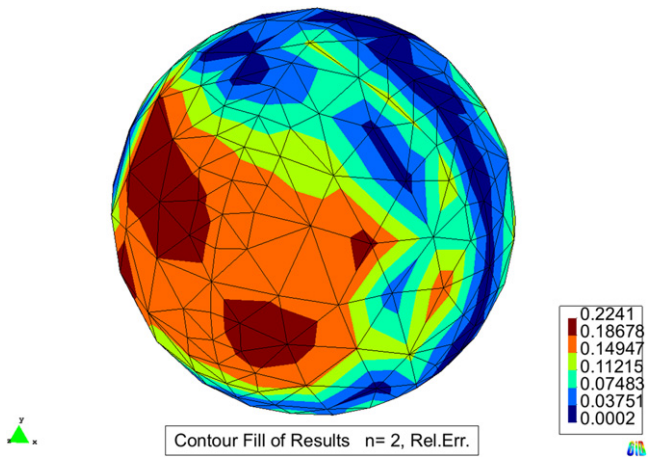

Fig. 15. The relative error in % ($k = 1$). Coarse mesh.

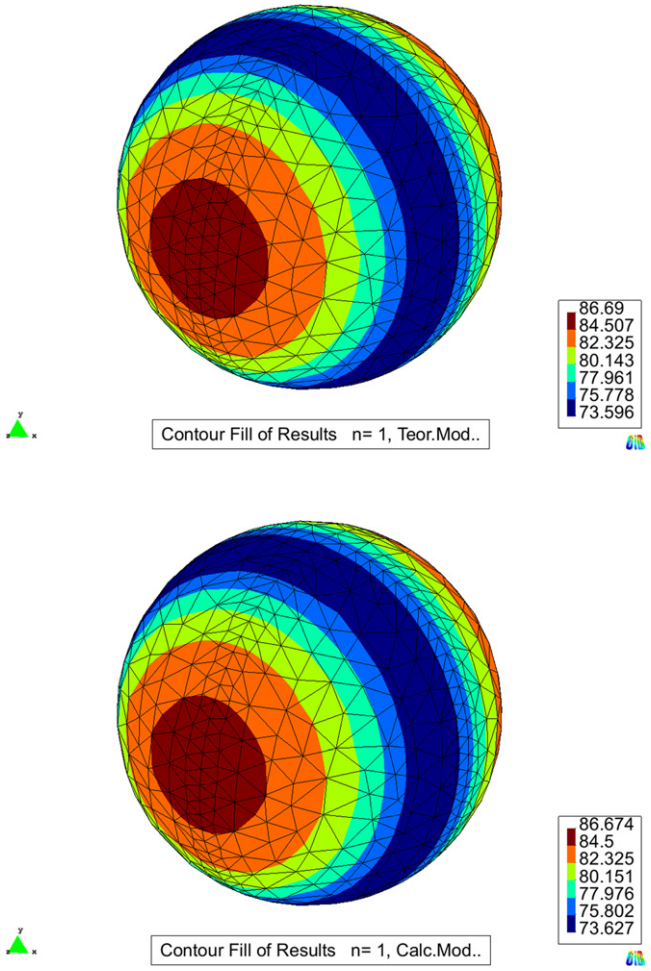

Fig. 16. Analytical and calculated pressure moduli ($k = 1$). Medium mesh.

with

$$
\begin{aligned}
M_i^*(r,\theta,\varphi) &= \sum_{m=0}^{\infty} w_m(k,r) \sum_{n=0}^{m} \left(A_{mn}^i Y_{mn}^1(\theta,\varphi) + B_{mn}^i Y_{mn}^{-1}(\theta,\varphi)\right) \\
\frac{\partial M_i^*}{\partial r} &= \sum_{m=0}^{\infty} \frac{\partial w_m}{\partial r} \sum_{n=0}^{m} \left(A_{mn}^i Y_{mn}^1 + B_{mn}^i Y_{mn}^{-1}\right) \\
\frac{\partial M_i^*}{\partial \theta} &= \sum_{m=0}^{\infty} w_m(k,r) \sum_{n=0}^{m} \left(A_{mn}^i \frac{\partial Y_{mn}^1}{\partial \theta} + B_{mn}^i \frac{\partial Y_{mn}^{-1}}{\partial \theta}\right) \\
\frac{\partial M_i^*}{\partial \varphi} &= \sum_{m=0}^{\infty} w_m(k,r) \sum_{n=0}^{m} \left(A_{mn}^i \frac{\partial Y_{mn}^1}{\partial \varphi} + B_{mn}^i \frac{\partial Y_{mn}^{-1}}{\partial \varphi}\right).
\end{aligned}
\tag{26}
$$

At this stage of the formulation, it must be pointed out that both trial and test functions have been written in terms of two *analytical* function families – Hankel functions and spherical harmonics – and the *constant* coefficients A_{mn}^i and B_{mn}^i. Hankel functions depend exclusively on the radius r and the wave number k; spherical harmonics, exclusively on the zenithal and azimuthal angles θ and φ. The next step of the formulation (Section 3.3.2) is the substitution of trial functions of (25) and test functions of (26) in the weak formulation (12). The fact that in Eqs. (25) and (26) only analytical functions (Hankel functions and spherical harmonics) and constants (A_{mn}^i and B_{mn}^i) appear will allow for the calculation of the integrals to be analytic: some of those integrals – those involving Hankel functions – will be line integrals from a to ∞; others – those involving spherical harmonics – will be double integrals over the surface S.

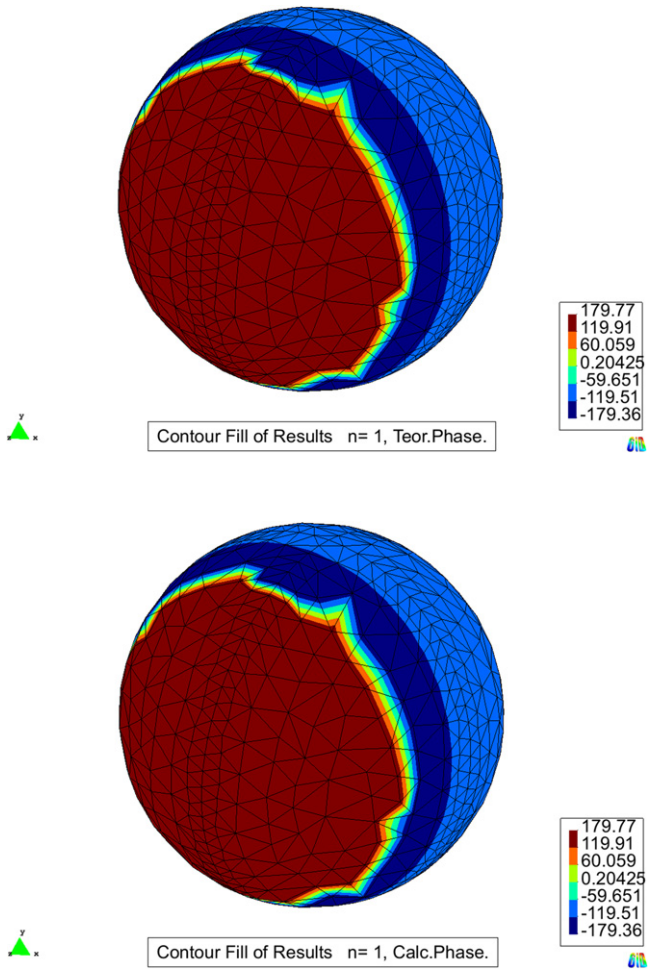

Fig. 17. Analytical and calculated pressure phases ($k = 1$). Medium mesh.

Regarding the space of test functions $w(r, \theta, \varphi) \in C_w^{\infty}(\Omega_s)$, two alternatives have been compared: a weighted space which comprises functions

$$w_m(k, r) = \frac{1}{r^2} h_m(k, r) = e^{ikr} \frac{i^{-(m+1)}}{kr^2} \sum_{t=0}^{m} \frac{(m+t)!}{(m-t)!t!} \left(\frac{i}{2k}\right)^t r^{-t} \tag{27}$$

and a weighted conjugated one, which comprises functions

$$w_m(k, r) = \frac{1}{r^2} \overline{h_m(k, r)} = (-1)^{m+1} e^{-ikr} \frac{i^{-(m+1)}}{kr^3} \sum_{t=0}^{m} \frac{(-1)^t (m+t)!}{(m-t)!t!} \left(\frac{i}{2k}\right)^t r^{-t}. \tag{28}$$

3.3.2. Matrix formulation

Rewriting the variational formulation (12) in spherical coordinates and substituting the functions (25) and (26), we obtain the coefficients of the global K stiffness matrix:

$$\begin{aligned} K_{ij} &= \iiint_{\Omega_s} \vec{\nabla} M_i^*(r, \theta, \varphi) \, \vec{\nabla} M_j(r, \theta, \varphi) \, d\Omega \\ &= \iiint_{\Omega_s} \left(\sum_{m=0}^{\infty} \sum_{n=0}^{m} \left(A_{mn}^i Y_{mn}^1 + B_{mn}^i Y_{mn}^{-1} \right) \frac{\partial w_m}{\partial r} \right) \left(\sum_{d=0}^{\infty} \sum_{l=0}^{d} \left(A_{dl}^j Y_{dl}^1 + B_{dl}^j Y_{dl}^{-1} \right) \frac{\partial h_d}{\partial r} \right) d\Omega \end{aligned}$$

$$+\iiint_{\Omega_s}\frac{1}{r^2}\left(\sum_{m=0}^{\infty}\sum_{n=0}^{m}\left(A_{mn}^{i}\frac{\partial Y_{mn}^{1}}{\partial\theta}+B_{mn}^{i}\frac{\partial Y_{mn}^{-1}}{\partial\theta}\right)w_m\right)\left(\sum_{d=0}^{\infty}\sum_{l=0}^{d}\left(A_{dl}^{j}\frac{\partial Y_{dl}^{1}}{\partial\theta}+B_{dl}^{j}\frac{\partial Y_{dl}^{-1}}{\partial\theta}\right)h_d\right)d\Omega$$
$$+\iiint_{\Omega_s}\frac{1}{r^2\sin^2\theta}\left(\sum_{m=0}^{\infty}\sum_{n=0}^{m}\left(A_{mn}^{i}\frac{\partial Y_{mn}^{1}}{\partial\varphi}+B_{mn}^{i}\frac{\partial Y_{mn}^{-1}}{\partial\varphi}\right)w_m\right)\left(\sum_{d=0}^{\infty}\sum_{l=0}^{d}\left(A_{dl}^{j}\frac{\partial Y_{dl}^{1}}{\partial\varphi}+B_{dl}^{j}\frac{\partial Y_{dl}^{-1}}{\partial\varphi}\right)h_d\right)d\Omega.$$

And analogously for the coefficients of the M mass matrix:

$$M_{ij}=\iiint_{\Omega_s}M_i^{*}(r,\theta,\varphi)\,M_j(r,\theta,\varphi)\,d\Omega$$
$$=\iiint_{\Omega_s}\left(\sum_{m=0}^{\infty}\sum_{n=0}^{m}\left(A_{mn}^{i}Y_{mn}^{1}+B_{mn}^{i}Y_{mn}^{-1}\right)w_m\right)\left(\sum_{d=0}^{\infty}\sum_{l=0}^{d}\left(A_{dl}^{j}Y_{dl}^{1}+B_{dl}^{j}Y_{dl}^{-1}\right)h_d\right)d\Omega.$$

Taking into account the orthogonality of the spherical harmonics $Y_{mn}^{\sigma}(\theta,\varphi)$ and its derivatives, we can directly write the formulas for the coefficients of the global stiffness matrix

$$K_{ij}=\sum_{m=0}^{\infty}I_{m1}\sum_{n=0}^{m}\left(A_{mn}^{i}A_{mn}^{j}I_0^{1}+B_{mn}^{i}B_{mn}^{j}I_0^{-1}\right)+\sum_{m=0}^{\infty}I_{m2}\sum_{n=0}^{m}\left(A_{mn}^{i}A_{mn}^{j}I_\theta^{1}+B_{mn}^{i}B_{mn}^{j}I_\theta^{-1}\right)$$
$$+\sum_{m=0}^{\infty}I_{m2}\sum_{n=0}^{m}\left(A_{mn}^{i}A_{mn}^{j}I_\varphi^{1}+B_{mn}^{i}B_{mn}^{j}I_\varphi^{-1}\right)\tag{29}$$

and the coefficients of the global mass matrix

$$M_{ij}=\sum_{m=0}^{\infty}I_{m3}\sum_{n=0}^{m}\left(A_{mn}^{i}A_{mn}^{j}I_0^{1}+B_{mn}^{i}B_{mn}^{j}I_0^{-1}\right).\tag{30}$$

In the latter formulas, the double integrals of the spherical harmonics and their derivatives are defined as

$$\begin{aligned}
I_0^{1}(m,n)&=\int_0^{2\pi}d\varphi\int_0^{\pi}\left(Y_{mn}^{1}\right)^2\sin\theta\,d\theta,\\
I_0^{-1}(m,n)&=\int_0^{2\pi}d\varphi\int_0^{\pi}\left(Y_{mn}^{-1}\right)^2\sin\theta\,d\theta,\\
I_\theta^{1}(m,n)&=\int_0^{2\pi}d\varphi\int_0^{\pi}\left(\frac{\partial Y_{mn}^{1}}{\partial\theta}\right)^2\sin\theta\,d\theta,\\
I_\theta^{-1}(m,n)&=\int_0^{2\pi}d\varphi\int_0^{\pi}\left(\frac{\partial Y_{mn}^{-1}}{\partial\theta}\right)^2\sin\theta\,d\theta,\\
I_\varphi^{1}(m,n)&=\int_0^{2\pi}d\varphi\int_0^{\pi}\frac{1}{\sin\theta}\left(\frac{\partial Y_{mn}^{1}}{\partial\varphi}\right)^2d\theta,\\
I_\varphi^{-1}(m,n)&=\int_0^{2\pi}d\varphi\int_0^{\pi}\frac{1}{\sin\theta}\left(\frac{\partial Y_{mn}^{-1}}{\partial\varphi}\right)^2d\theta
\end{aligned}\tag{31}$$

and depend exclusively on the values of m and n; hence, they can be precomputed.

The line integrals of the Hankel and weight functions

$$\begin{aligned}
I_{m1}(k,a,m)&=\int_a^{\infty}r^2\frac{dw_m}{dr}\frac{dh_m}{dr}dr\\
I_{m2}(k,a,m)&=\int_a^{\infty}w_m(kr)\,h_m(kr)\,dr\\
I_{m3}(k,a,m)&=\int_a^{\infty}r^2w_m(kr)\,h_m(kr)\,dr,
\end{aligned}\tag{32}$$

depend on the wave number k, the radius a and m. In the work presented here, the analytical expressions of the three primitives have been calculated; however, although they can be exactly and simply evaluated, their values change with the frequency of the analysis.

Eqs. (29) and (30) provide the main advantage of the method proposed here: namely, that the FE *global* matrices of the outer mesh are directly calculated, without having to do any integration loop over the 2D elements on the surface S.

In practice, the proposed algorithm consists of the following phases.

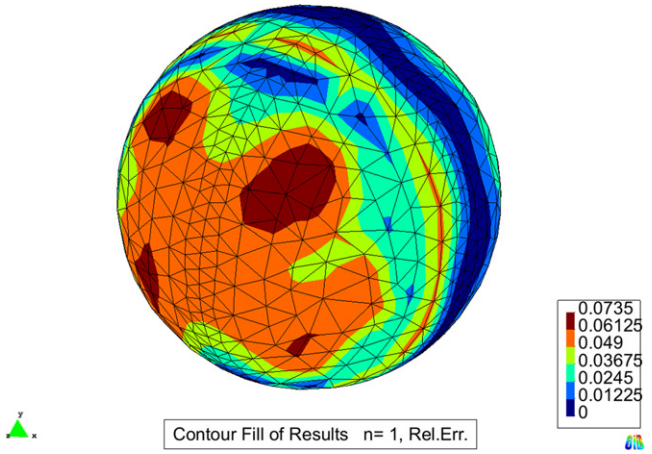

Fig. 18. The relative error in % ($k = 1$). Medium mesh.

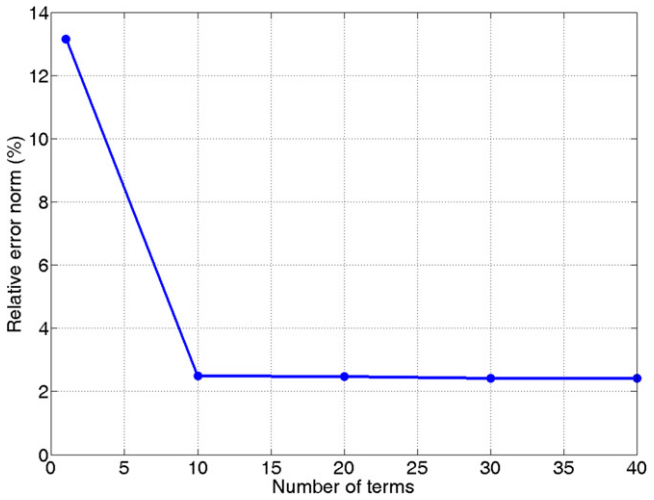

Fig. 19. The relative error (%) in the H^1 norm ($k = 1$). Coarse mesh.

- The integrals (31) are evaluated analytically once for all models and stored in memory.
- In the pre-process, performed only once for each model, coefficients (20) are computed and stored in memory.
- During the main computations, performed once for each model and frequency, the only calculations needed are: the *direct evaluation* of functions (32), the *matrix products* that give the full matrices K and M of (29) and (30), and the assembly procedure into the stiffness and mass matrices previously calculated for the inner subdomain Ω_i (coupled to the degrees of freedom associated to the nodes on the dividing surface S).

To summarize, no volume integral is needed in the calculations over the exterior domain. The use of (25) avoids the need of smoothing for the calculations of the values of the derivatives on the nodes and any post-process magnitude related to them. If the nodal values of the spherical harmonics (14) and their derivatives are calculated and stored in the pre-process, the post-processing of the pressure and its derivatives can be performed very quickly, once again by simple matrix products.

4. Numerical experiments

Two numerical experiments will be presented: one of radiation (a dipole) and one of scattering (scattering of a plane wave on a rigid sphere). The aim of the numerical experiments shown in this section is to check the validity of the formulation presented above. In the results that follow, the error between the analytical solution p and the numerical approximated solution p^h has been measured in the whole domain Ω by the weighted L^2 and H^1 norms:

$$\|p - p^h\|_0^2 = \iiint_{\Omega_i} |p - p^h|^2 d\Omega + + \iiint_{\Omega_s} \frac{1}{r^3} |p - p^h|^2 d\Omega, \tag{33}$$

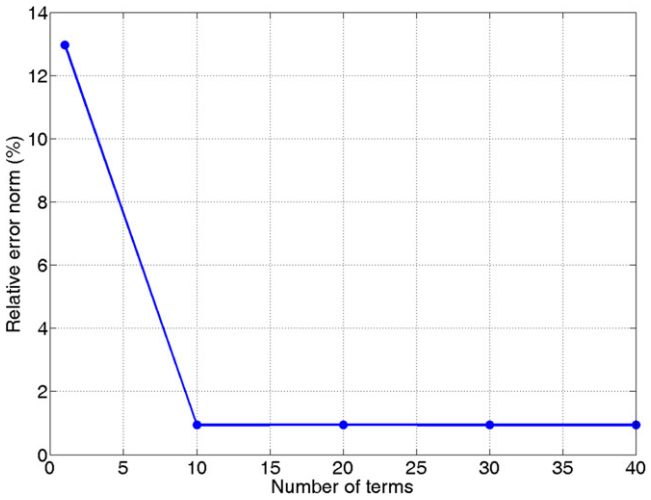

Fig. 20. The relative error (%) in the H^1 norm ($k = 1$). Medium mesh.

$$\|p - p^h\|_1^2 = \iiint_{\Omega_i} |p - p^h|^2 d\Omega + \iiint_{\Omega_i} |\vec{\nabla}\left(p - p^h\right)|^2 d\Omega + \iiint_{\Omega_s} \frac{1}{r^3} |p - p^h|^2 d\Omega + \iiint_{\Omega_s} \frac{1}{r^3} |\vec{\nabla}\left(p - p^h\right)|^2 d\Omega, \tag{34}$$

where the numerical approximated solution p^h and its gradient are calculated in the usual way in the subdomain Ω_i and using (25) in the subdomain Ω_s.

In all the results, the number of terms (theoretically infinite) of the summation over d of (25) has been truncated at a finite number of terms indicated by d_k. In the contour plots shown, the local relative error in percentage is always given by the modulus

$$E_r(r, \theta, \varphi) = 100 * abs\left(\frac{p - p^h}{p}\right). \tag{35}$$

4.1. Dipole radiation

The experiment consists of the simulation of the radiation from a dipole source located on the X axis. The distance between the two point sources (numerically modeled as small finite-size balls) is $d = 0.001$ m. The dividing surface has been located at a radius $a = 0.05$ m. The geometry of the model is shown in Fig. 2.

Two unstructured tetrahedral linear meshes have been used; one with 603 d.o.f. (114 of them located at the dividing surface) and a maximum edge size of 0.035 m, and another with 1340 d.o.f. (450 of them located at the dividing surface) and a maximum edge size of 0.029 m. For a wave number of $k = 10$, the dividing sphere is located at a distance of about $\lambda/13$ ($\lambda = 0.628$ m) from the center of the dipole. In order to have five nodes per wavelength, it would be advisable to use a maximum edge size of about 0.13 m, which provides a great margin for both coarse and fine meshes. To put the reliability of the method through an awkward position, the order of the coefficients calculated for spherical harmonics has been carried up to 25 in order to test the convergence of the method.

Figs. 3 and 4 show plots of the modulus (in Pa) and phase (in degrees), respectively, of the analytical and approximated solutions of the radiated pressure given by the coarse mesh at radius $r = 0.2$.

Fig. 5 shows the plot of the relative error (in %) corresponding to the approximated solutions of the radiated pressure at radius $r = 0.2$.

Figs. 6 and 7 display plots of the modulus (in Pa) and phase (in degrees), respectively, of the analytical and approximated solutions of the radiated pressure given by the finest mesh used at radius $r = 0.2$.

Fig. 8 describes the relative error (in %) committed by the approximated solutions of the radiated pressure at radius $r = 0.2$.

Finally, Figs. 9 and 10 show the values of the relative H^1 norms (natural scale) obtained, as a function of the truncation term in the summation over d of (25).

In Fig. 9, corresponding to the coarse mesh, the norm of the relative error has increased from $d_k = 1$ to $d_k = 25$; but a closer look at the scale suggests two observations: first, that the values are practically constant (they range between 0.66% and 0.68%); second, that the best values correspond to the spherical harmonics up to the smallest orders. This can be explained having a look at the similitude of the patterns of the quite simple analytical solution (Figs. 6 and 7) and that of

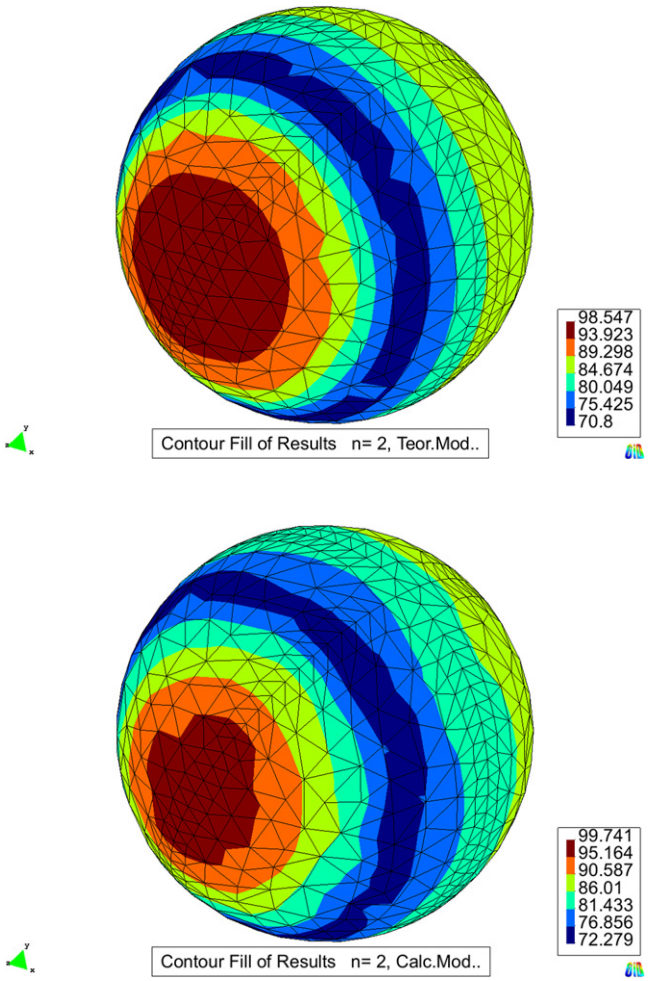

Fig. 21. Analytical and calculated pressure moduli ($k = 10$). Medium mesh.

spherical harmonic Y_{10}^1 (Fig. 11). The similitude suggests that only the smallest orders of spherical harmonics contribute to the numerical solution. The assertion that contributions of higher orders are negligible is confirmed by the negligible change in the norm; another confirmation is taken from the results obtained by the fine mesh (Fig. 10), where the norm increases again, but this time from one until the medium value, and decreases from there on. Once again, the scale indicates that, in practice, the error has not changed significantly.

The values of the relative H^1 norms show that the method has increased its accuracy as the mesh has been refined; besides, the errors remain (almost) constant as the order of the terms in the approximation is increased.

4.2. Scattering of a plane wave by a rigid sphere

4.2.1. The analytical solution

In this section, the benchmark model used for the test is the scattering of an incident plane wave traveling in the z-direction and finds in its way a rigid sphere of radius 1. The goal is to find the scattered wave p^s.

The equation of a plane wave is given by Morse and Ingard [26]

$$p^{inc}(r,\theta) = P_{\text{inc}} \sum_{m=0}^{\infty} (2m+1)\, i^n P_m(\cos\theta)\, j_m(k,r) \tag{36}$$

where P_{inc} is the amplitude of the incident wave, $P_m(\cos\theta)$ is the Legendre polynomial of degree m and $j_m(k,r)$ is the mth spherical Bessel function of the first kind.

The condition that relates the incident and the scattered wave is

$$-\frac{\partial p^s}{\partial r} = \frac{\partial p^{inc}}{\partial r} \quad \text{at } r = 1 \tag{37}$$

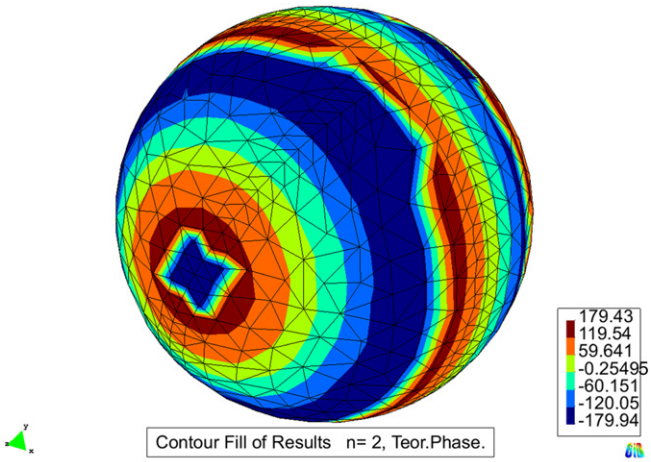

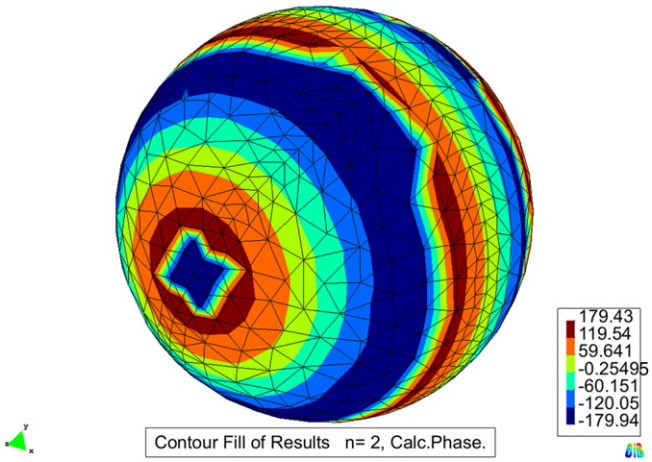

Fig. 22. Analytical and calculated pressure phases ($k = 10$). Medium mesh.

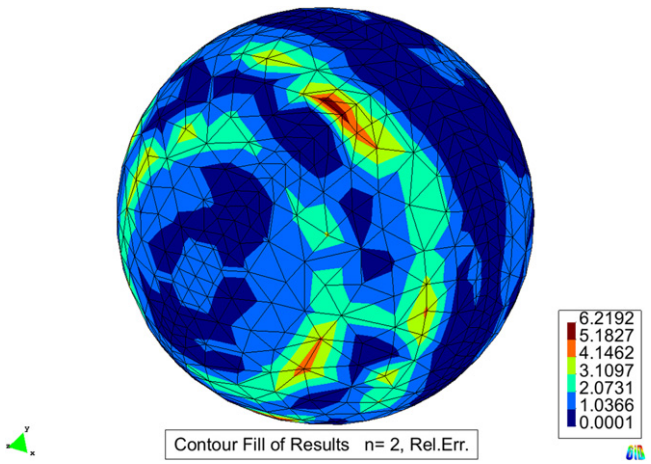

Fig. 23. The relative error in % ($k = 10$). Medium mesh.

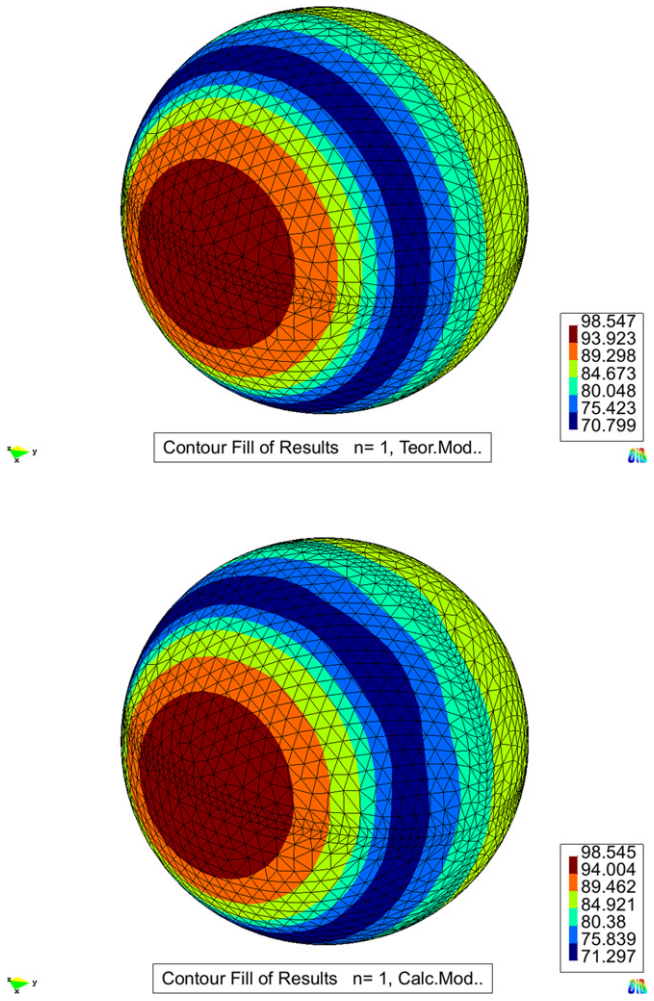

Fig. 24. Analytical and calculated pressure moduli ($k = 10$). Fine mesh.

where

$$\left.\frac{\partial p^{inc}}{\partial r}\right|_{r=1} = P_{\text{inc}} \sum_{m=0}^{\infty} (2m+1)\, i^m P_m(\cos\theta)\, \left.\frac{\partial j_m(k,r)}{\partial r}\right|_{r=1} \tag{38}$$

$$= \sum_{m=0}^{\infty}\sum_{n=0}^{n} P_m^n(\cos\theta)\left(\widetilde{A}_{mn}\cos(n\varphi) + \widetilde{B}_{mn}\sin(n\varphi)\right). \tag{39}$$

Assuming the Neumann boundary condition and the orthogonality properties of functions $P_m^n(\cos\theta)$ and cos and sin functions, we obtain the following relationships between the coefficients

$$\widetilde{B}_{mn} = 0 \quad \forall m, n$$
$$\widetilde{A}_{mn} = 0 \quad \forall n \geq 1$$
$$\widetilde{A}_{m0} = \widetilde{A}_m = P_{\text{inc}}\,(2m+1)\, i^m \left.\frac{\partial j_m(k,r)}{\partial r}\right|_{r=1} \quad \forall m \geq 1.$$

Finally, using Eq. (5) we have the analytical pattern for the scattered wave:

$$p^s(r,\theta) = \sum_{m=0}^{\infty} h_m(k,r)\, P_m(\cos\theta)\, A_m \tag{40}$$

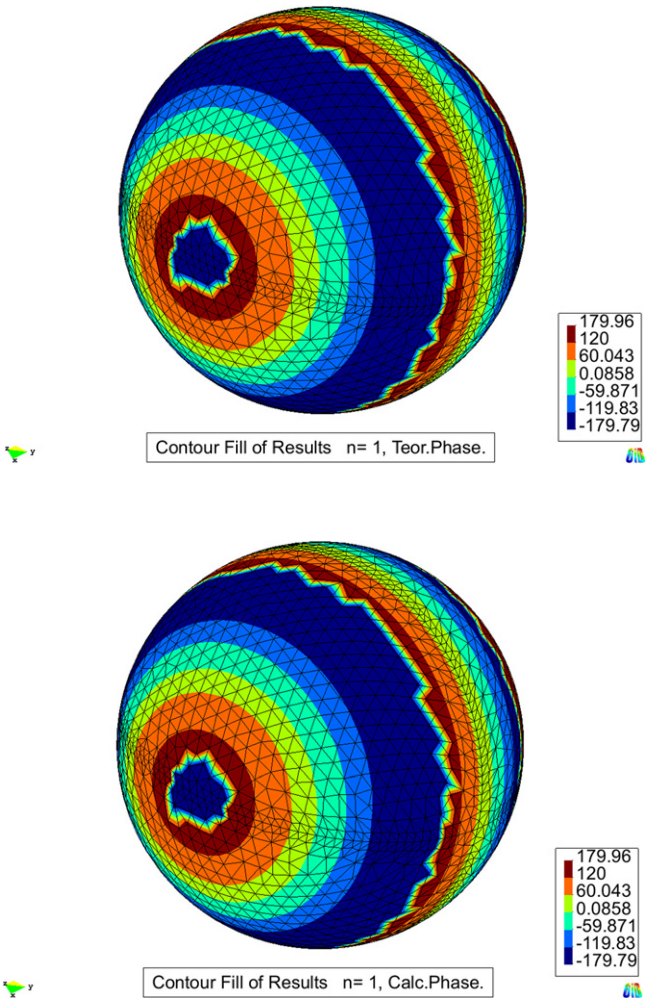

Fig. 25. Analytical and calculated pressure phases ($k = 10$). Fine mesh.

where

$$A_m = \frac{-P_{\text{inc}}\,(2m+1)\,i^m\,\frac{\partial j_m(k,r)}{\partial r}\Big|_{r=1}}{\frac{\partial h_m(k,r)}{\partial r}\Big|_{r=1}} \quad \forall m \geq 1.$$

The model has been tested for two different wave numbers: a lower one $k = 1$ (wavelength 6.28 m) and a higher one $k = 10$ (wavelength 0.628 m). Three different unstructured tetrahedral linear meshes corresponding to the same geometrical model have been used: a coarse one with a maximum edge size of 0.501 m and 427 d.o.f. (238 of them located at the dividing surface), a medium mesh with a maximum edge size of 0.348 m and 1292 d.o.f. (690 of them located at the dividing surface) and a fine one, with a maximum edge size of 0.196 m and 4546 d.o.f. (2376 of them located at the dividing surface). The geometrical model can be seen in Fig. 12. The dividing sphere has been set to $a = 1.1$ m, and the summation index of m in (40) has been set to 15. As in the previous example of Section 4.1, in order to test the reliability of the method, the order of the coefficients calculated for spherical harmonics has been carried up to 40 in order to check the behavior of the norms.

4.2.2. The first example: low wave number ($k = 1$)

For $k = 1$, the dividing sphere is located at a distance of about $\lambda/6$ from the scattering surface. In order to have five nodes per wavelength, it would be advisable to use a maximum edge size of about 1.26 m. This allows for a good margin for the size of the mesh, and quite good results are expected even for the coarse one.

Figs. 13 and 14 display plots of the modulus (in dB) and phase (in degrees), respectively, of the analytical and approximated solutions of the scattered pressure given by the coarse mesh at radius $r = 1.25$.

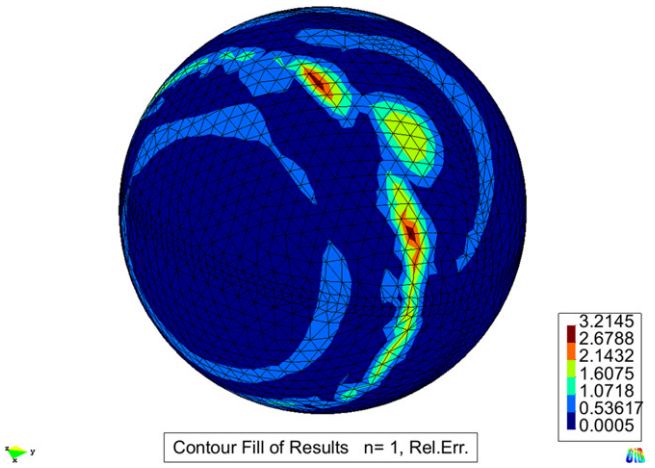

Fig. 26. The relative error in % ($k = 10$). Fine mesh.

Fig. 15 describes the relative error (in %) corresponding to the approximated solution of the scattered pressure given by the coarse mesh at radius $r = 1.25$.

Figs. 16 and 17 show plots of the modulus (in dB) and phase (in degrees), respectively, of the analytical and approximated solutions of the scattered pressure given by the medium mesh at radius $r = 1.25$.

Fig. 18 describes the relative error (in %) corresponding to the approximated solution given by the medium mesh at radius $r = 1.25$.

Figs. 19 and 20 display the values of the relative H^1 norms (natural scale) obtained using these two meshes, as a function of the truncation term in the summation over d of (25).

The results are quite accurate. The low frequency originates a quite smooth pattern for the scattered pressure, and the great margin for the edge size in the mesh allows even the coarse mesh to give acceptable results.

As in the previous example, it is remarkable that the norms have not destabilized as the order of the terms in the approximation has been increased. This time the pattern of the analytical solution (40) is complex enough to require higher orders of approximation than in the previous example.

4.2.3. The second example: high wave number ($k = 10$)

For $k = 10$, the dividing sphere is located at a distance of about $\lambda/6$ from the scattering surface. It would be advisable to use a maximum edge size of about 0.13 m. This presages a bad result for the medium mesh and a rather good one for the fine one.

Figs. 21 and 22 display plots of the modulus (in dB) and phase (in degrees), respectively, of the analytical and approximated solutions of the scattered pressure given by the medium mesh at radius $r = 1.25$.

Fig. 23 describes the relative error (in %) corresponding to the approximated solution of the scattered pressure given by the medium mesh at radius $r = 1.25$.

Figs. 24 and 25 show plots of the modulus (in dB) and phase (in degrees), respectively, of the analytical and approximated solutions of the scattered pressure given by the finer mesh used at radius $r = 1.25$.

Fig. 26 describes the relative error (in %) corresponding to the approximated solution given by the fine mesh at radius $r = 1.25$.

Figs. 27 and 28 show the values of the relative H^1 norms (natural scale) obtained using these two meshes, as a function of the truncation term in the summation over d of (25).

For this frequency, as has been predicted, the results are unacceptable for the medium mesh; but as the edge size has been reduced to a reasonable size in the fine mesh, the results become quite accurate. Moreover, as Fig. 26 shows, the relative error is quite small except on the plane where the most abrupt change of the pressure takes place; this would be the plane where adaptive meshing would mostly refine the mesh.

As in the two previous examples, it is again remarkable that the norms have not destabilized as the order of the terms in the approximation has been increased.

5. Conclusions and future work

A method for the resolution of the Helmholtz equation in interior and exterior domains has been presented. The proposed approximation uses an analytical pattern for the interpolation on the radial direction and a series expansion of the FE trial and test functions for the interpolation on the zenithal and azimuthal directions.

From the methodology and the results obtained, the following conclusions may be drawn.

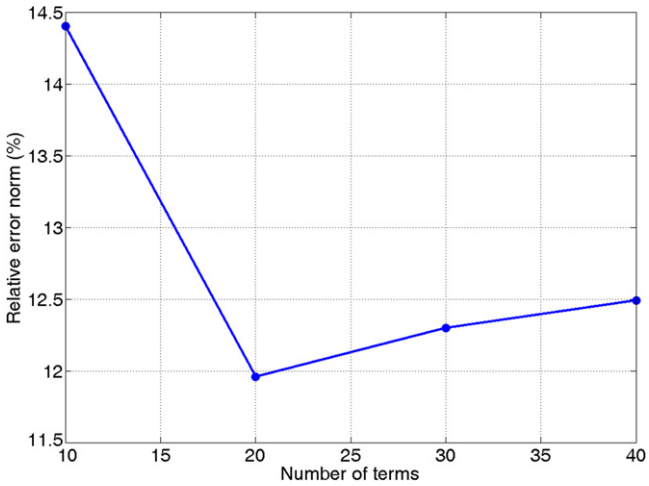

Fig. 27. The relative error (%) in the H^1 norm ($k = 10$). Medium mesh.

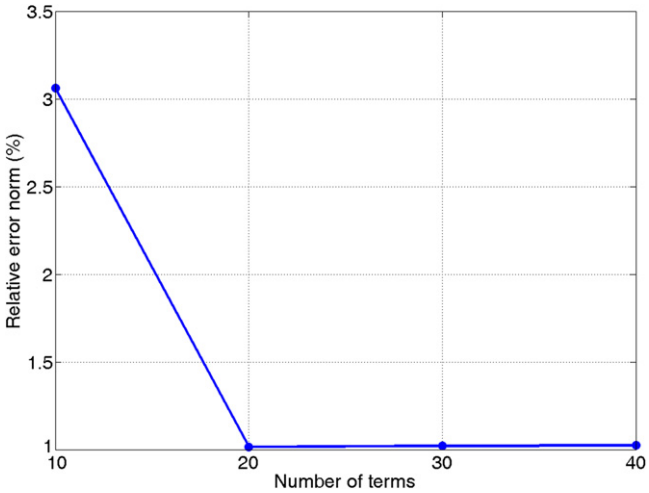

Fig. 28. The relative error (%) in the H^1 norm ($k = 10$). Fine mesh.

- As has been already pointed out in Section 3.3.2, the proposed method is computationally efficient, since only evaluations of functions and single matrix products must be performed for the calculation of the global matrices.
- The dividing surface can be located close to the radiator or scatterer—in the near field. This minimizes the number of degrees of freedom of the mesh.
- No discretization is needed for the outer subdomain; therefore, no additional degrees of freedom are added, and the inner and outer meshes are assembled naturally, as in any ordinary finite element method.
- The radiation condition at infinity is exactly satisfied when modeling unbounded (infinite or semi-infinite) domains.
- No approximation other than that of the 2D finite elements on the dividing surface is introduced.
- The method avoids – in the outer domain – the need of smoothing for the post-processing of the derivatives of the acoustic pressure, which are directly calculated. This allows for an easy computation of magnitudes related to the derivatives (particle velocity, intensity, power, etc.).
- The presented analysis and numerical results – steadiness of the norms – indicate that solutions stabilize as the number of terms used in the series expansion increases, accounting for the reliability of the method.
- No appreciable differences have been detected comparing the results obtained using the weighted symmetrical and conjugated test functions detailed in Section 3.3.1.

The proposed methodology has to be analyzed for structural/fluid and other couplings and differential equations other than Helmholtz's. The authors expect to present further theoretical and numerical results in a forthcoming work.

Acknowledgments

The authors thank the Basque Government for its financial assistance through IT-453-10, as well as the University of The Basque Country (UPV/EHU) for its financial support through UFI11/29. The fourth author was partially funded by the Project of the Spanish Ministry of Sciences and Innovation MTM2010-16511, the Laboratory of Mathematics (UFI 11/52), and the Ibero-American Project CYTED 2011 (P711RT0278).

References

[1] R.D. Ciskowski, C.A. Brebbia, Boundary Element Methods in Acoustics, Computational Mechanics Publications and Elsevier Applied Science, 1991.
[2] M.M. Grigoriev, G.F. Dargush, A fast multi-level boundary element method for the Helmholtz equation, Computer Methods in Applied Mechanics and Engineering 193 (2004) 165–203.
[3] L. Demkowicz, J.T. Oden, Recent progress on application of hp-adaptive be/fe methods to elastic scattering, International Journal for Numerical Methods in Engineering (1994).
[4] M.G. Blyth, C. Pozridikis, A comparative study of the boundary and finite element methods for the Helmholtz equation in two dimensions, Engineering Analysis with Boundary Elements 31 (2007) 35–49.
[5] P. Bettess, Infinite Elements, Penshaw Press, 1992.
[6] R.J. Astley, G.J. Macaulay, J.P. Coyette, Mapped wave envelope elements for acoustical radiation and scattering, Journal of Sound and Vibration 170 (1) (1994) 97–118.
[7] K. Gerdes, L. Demkowicz, Solution of 3D-Laplace and Helmholtz equations in exterior domains using hp-infinite elements, Computer Methods in Applied Mechanics and Engineering 137 (1) (1996) 239–273.
[8] K. Gerdes, A summary of infinite element formulations for exterior Helmholtz problems, Computer Methods in Applied Mechanics and Engineering 164 (1998) 95–105.
[9] W. Bangerth, M. Grote, C. Hohenegger, Finite element method for time dependent scattering: nonreflecting boundary condition, adaptivity, and energy decay, Computer Methods in Applied Mechanics and Engineering 193 (2004) 2453–2482.
[10] S. Thirunavukkarasu, N. Murthy, Absorbing boundary conditions for time harmonic wave propagation in discretized domains, Computer Methods in Applied Mechanics and Engineering 200 (2011) 2483–2497.
[11] X. Antoine, M. Darbas, Y. Lu, An improved surface radiation condition for high-frequency acoustic scattering problems, Computer Methods in Applied Mechanics and Engineering 195 (2006) 4060–4074.
[12] T. Hagstrom, M.O. Assaf, D. Givoli, High-order local absorbing conditions for the wave equation: extensions and improvements, Journal of Computational Physics 227 (2008) 3322–3357.
[13] R. Huan, L.L. Thompson, Accurate radiation boundary conditions for the time-dependent wave equation on unbounded domains, International Journal for Numerical Methods in Engineering 47 (2000) 1569–1603.
[14] L.L. Thompson, R. Huan, Accurate radiation boundary conditions for the two-dimensional wave equation on unbounded domains, Computer Methods in Applied Mechanics and Engineering 191 (2001) 311–351.
[15] H. Harari, U. Albocher, Studies of fe/pml for exterior problems of time-harmonic elastic waves, Computer Methods in Applied Mechanics and Engineering 195 (2006) 3854–3879.
[16] J. Diaz, P. Poly, A time domain analysis of pml models in acoustics, Computer Methods in Applied Mechanics and Engineering 195 (2006) 3820–3853.
[17] J.J. Shirron, T.E. Giddings, A finite element model for acoustic scattering from objects near a fluid–fluid interface, Computer Methods in Applied Mechanics and Engineering 196 (2006) 279–288.
[18] X. Jiang, Z. Weiying, Adaptive perfectly matched layer method for multiple scattering problems, Computer Methods in Applied Mechanics and Engineering 201–204 (2012) 42–52.
[19] J.P. Wolf, The Scaled Boundary Finite Element Method, Penshaw Press, 2003.
[20] S. Chongmin, J.P. Wolf, The scaled boundary finite element method: analytical solution in frequency domain, Computer Methods in Applied Mechanics and Engineering 164 (1998) 249–264.
[21] J.P. Wolf, S. Chongmin, The scaled boundary finite element method? A fundamental solution-less boundary-element method, Computer Methods in Applied Mechanics and Engineering 190 (2001) 5551–5568.
[22] L.E. García-Castillo, I. Gómez-Revuelto, M. Salazar-Palma, A finite element method for the analysis of radiation and scattering of electromagnetic waves on complex environments, Computer Methods in Applied Mechanics and Engineering 194 (2–5) (2005) 637–655.
[23] I. Gómez-Revuelto, L.E. García-Castillo, M. Salazar-Palma, Tapan K. Sarkar, Fully coupled hybrid method FEM/high-frequency technique for the analysis of radiation and scattering problems, Microwave and Optical Technology Letters 47 (2005) 104–107.
[24] I. Gómez-Revuelto, L.E. García-Castillo, L.F. Demkowicz, A comparison between PML, infinite elements and an iterative BEM as mesh truncation methods for hp self-adaptive procedures in electromagnetics, Progress in Electromagnetics Research 126 (2012) 499–519.
[25] P.M. Morse, H. Feshbach, Methods of Theoretical Physics, McGraw-Hill Book Company, 1953.
[26] P.M. Morse, K.U. Ingard, Theoretical Acoustics Vols. 1–2, McGraw-Hill Book Company, 1968.
[27] L. Grasedyck, W. Hackbusch, Construction and arithmetics of H-matrices, Computing 70 (4) (2003) 295–334.
[28] P.G. Schmitz, L. Ying, A fast direct solver for elliptic problems on Cartesian meshes in 3D. http://www.math.utexas.edu/users/lexing/publications/direct3d.pdf.
[29] P. Goransson, Acoustic finite elements, Course on Advanced Techniques in Applied and Numerical Acoustics, Katholieke Universiteit Leuven, Haverlee, Belgium, 1988.
[30] P. Goransson, A symmetric finite element formulation for fluid–structure interaction analysis, Journal of Sound and Vibration 123 (3) (1988) 507–515.
[31] I. Harari, K. Grosh, T.J.R. Hughes, M. Malhotra, J.R. Pinsky, J.R. Stewart, L.L. Thompson, Recent development in finite element methods for structural acoustics, Archives of Computational Methods in Engineering 3 (2–3) (1996) 131–310.
[32] R. Leis, Initial Value Problems in Mathematical Physics, Teubner, 1986.
[33] D.S. Burnett, A three-dimensional acoustic infinite element based on a prolate spheroidal multipole expansion, Journal of the Acoustical Society of America 96 (1994) 2798–2816.